ASM Handbook, Volume 24A, *Additive Manufacturing Design and Applications*
M. Seifi, D. Bourell, W. Frazier, H. Kuhn, editors
DOI 10.31399/asm.hb.v24A.a0006954

In-Process Thermography of Metal Additive Manufacturing Processes

Brandon Lane and David Deisenroth, National Institute of Standards and Technology (NIST)

Historical Background

Temperature measurement of manufacturing processes has a long history (Ref 1). While the ultimate goal of the measurement may not be to understand temperature itself, temperature is a basic characteristic of thermal energy transfer and fundamental to understanding a myriad physical phenomena that affect the performance or quality of a manufacturing process. Temperature-measurement methods vary widely, but only thermography provides simultaneous spatial, temporal, and temperature information.

The application of thermography in additive manufacturing (AM) is still largely a research and development (R&D) endeavor, because many aspects of metal AM processes pose unique and substantial metrological challenges. This article aims to provide readers with a brief review of current applications of thermography in AM, with particular focus on metals-based laser powder-bed fusion (L-PBF), although applications in directed-energy deposition (DED) and electron beam PBF (E-PBF) are mentioned. Temperature metrology adds an additional layer of complexity, in contrast to high-speed imaging, machine vision, photogrammetry, and so on. A basic theoretical background on radiation thermometry is provided, with notes on how the various equations are applied. Finally, specific examples and lessons learned from various AM thermographic studies at the National Institute of Standards and Technology (NIST) are provided.

Certain commercial equipment, instruments, or materials are identified in this article, to adequately specify the experimental procedure. Such identification is not intended to imply recommendation or endorsement by NIST, nor is it intended to imply that the materials or equipment identified are necessarily the best available for the purpose. These opinions, recommendations, findings, and conclusions do not necessarily reflect the views or policies of NIST or the U.S. government.

Melt Pools—Size, Scale, and Temperatures

The design of a measurement system may seem like a chicken-or-egg problem, in that one must know something about a measurement before designing the measurement system or interpreting results from that system. Likewise, AM thermographers should have an idea of the relative spatial, temporal, radiant emission, and temperature characteristics of their measured object or phenomena of interest (i.e., the measurand) before they endeavor to measure temperature. The relative geometric scales of metal AM melt pools are highly dependent on the process type (e.g., L-PBF, E-PBF, or DED), the processing parameters (e.g., laser spot size, power, scan speed, or scan sequence), and material. In general, the width of a melt pool is the same length scale and slightly larger than the width of the thermal energy source. For L-PBF, which typically results in smaller-scale melt pools than E-PBF or DED, this is on the order of 100 μm in width and 1 mm (0.4 in.) in length (Fig. 1). For highly thermally conductive materials such as aluminum, melt pool sizes may be significantly smaller. Generally, the size and scale of a melt pool dynamically fluctuates during fabrication, largely dependent on the interactions of scan strategy, part geometry, or varying processing parameters.

In manufacturing production, thermal imaging is most often required to cover the entire build area or part. Obtaining melt-pool-scale imaging resolution (approximately 50 μm/pixel or less) over such large areas (commonly approximately 250^2 mm^2 or more) requires substantially large image formats (approximately 20 megapixel or more) and inevitably large data volumes collected over multihour builds. Similar data volume calculations are provided by AM researchers (Ref 2, 3).

It is somewhat more difficult to associate a specific temporal scale for metal AM processes, because many of the physical phenomena are relatively high speed, chaotic, nondeterministic, and nonharmonic. However, total AM build times can exceed dozens of hours. Temporal rates are often provided relative to some characteristic scale, such as $f = v/d$, where f is the frequency in Hertz of some target phenomenon, v is some characteristic speed, and d is some characteristic distance. For example, a typical L-PBF laser scan speed of v = 1 m/s (3.3 ft/s) and laser spot diameter of d = 85 μm means that the laser will traverse its own spot diameter at approximately 11.7 kHz. The same laser scanning a hatch pattern (e.g., stripe) width of d = 5 mm (0.2 in.) may elicit a signature frequency of 200 Hz.

Temperature scales range from near ambient to above the boiling point of metals, all within a short scale, resulting in exceedingly high thermal gradients and heating/cooling rates. These temperature range and thermal gradient scales pose significant metrological challenges for thermal imaging due to various instrument limitations and finite measurable temperature ranges (see the section "Detector Linearity and Dynamic Range" in this article), in addition to the short scales and temporal rates previously mentioned.

Thermographic Setups in Additive Manufacturing Research

In the last 5 to 10 years, metals AM in situ process-monitoring research has grown significantly, resulting in many excellent reviews on the subject (Ref 3–11). Because thermal measurements are a critical aspect of in situ monitoring, many of these articles focus on thermographic applications in AM. These reviews also try to categorize and group similar applications or techniques. One primary classification is based on relative optical positioning of a camera with respect to the fabrication process.

If a camera and associated optics are mounted at a fixed position relative the build area, it is said to be a staring, off-axis, or off-axial configuration. A staring configuration may be considered the most standard configuration for thermal imagers. Another common

configuration in L-PBF and laser-based DED, which is relatively unique to AM and stems from earlier work in laser welding, places the camera so that it shares the same optical path as the processing laser. As a result, the laser spot and melt pool remain fixed within the field of view of the camera. A beam splitter is used to separate the laser wavelength from the visible (VIS) spectrum or other wavelengths observed by the camera. These configurations are called coaxial, on-axis, or down beam. Examples and special considerations for coaxial system thermography are discussed in the section "Coaxial System Design Challenges" in this article. Generally, coaxial systems are only found on L-PBF and DED systems. The E-PBF systems cannot employ coaxial imaging systems because a camera optical path is not steerable via the same deflector coils that steer the electron beam. However, thermal imagers can be affixed to the motion axes of larger-scale e-beam, laser, or polymer-based DED systems so that the heated region is retained within the imager field of view, similar to laser coaxial methods (Ref 12–14).

Apart from the optical configuration, reviews often characterize AM thermography systems by the observed "scene," such as the example melt-pool-scale and part-scale thermal images in Fig. 1. In another example, Mazzoleni et al. categorized these as melt pool monitoring and whole-build platform monitoring (Ref 3). Finally, AM thermographic setups are commonly characterized by their end use or application and typically cited in the context of process monitoring, quality control, or defect detection. However, applications in AM are more widespread and overlapping and may be categorized as:

- *Process monitoring and quality control:* These applications aim to use thermography or various other measurement systems during fabrication to monitor or predict fabrication quality. The majority of AM thermography R&D is geared toward process monitoring or control, as demonstrated in the prior list of reviews. These applications may require practicality more than metrological accuracy. Most require indication of processing stability or anomalies and not temperature calibration or indication of temperature values.
- *Model/simulation development and validation:* Various model types or AM simulations are either in R&D or available as commercial products (Ref 15–19). Many of these predict and use temperature fields as a precursor to other phenomena, such as solidification or residual strain and part distortion. Thermography applications for AM model/simulation development typically require more stringent metrological considerations and thermal calibration to achieve indication of real physical values (e.g., temperature, distance, time, etc.).
- *Underlying physical, fundamental, or phenomenological studies:* These applications are primarily fundamental research intended to explore the interplay of the many physical phenomena that occur in metal AM. Similar to model validation, these endeavors often require stringent metrological considerations to achieve accurate indications of real physical values. Results from this research are valuable to either of the aforementioned applications.

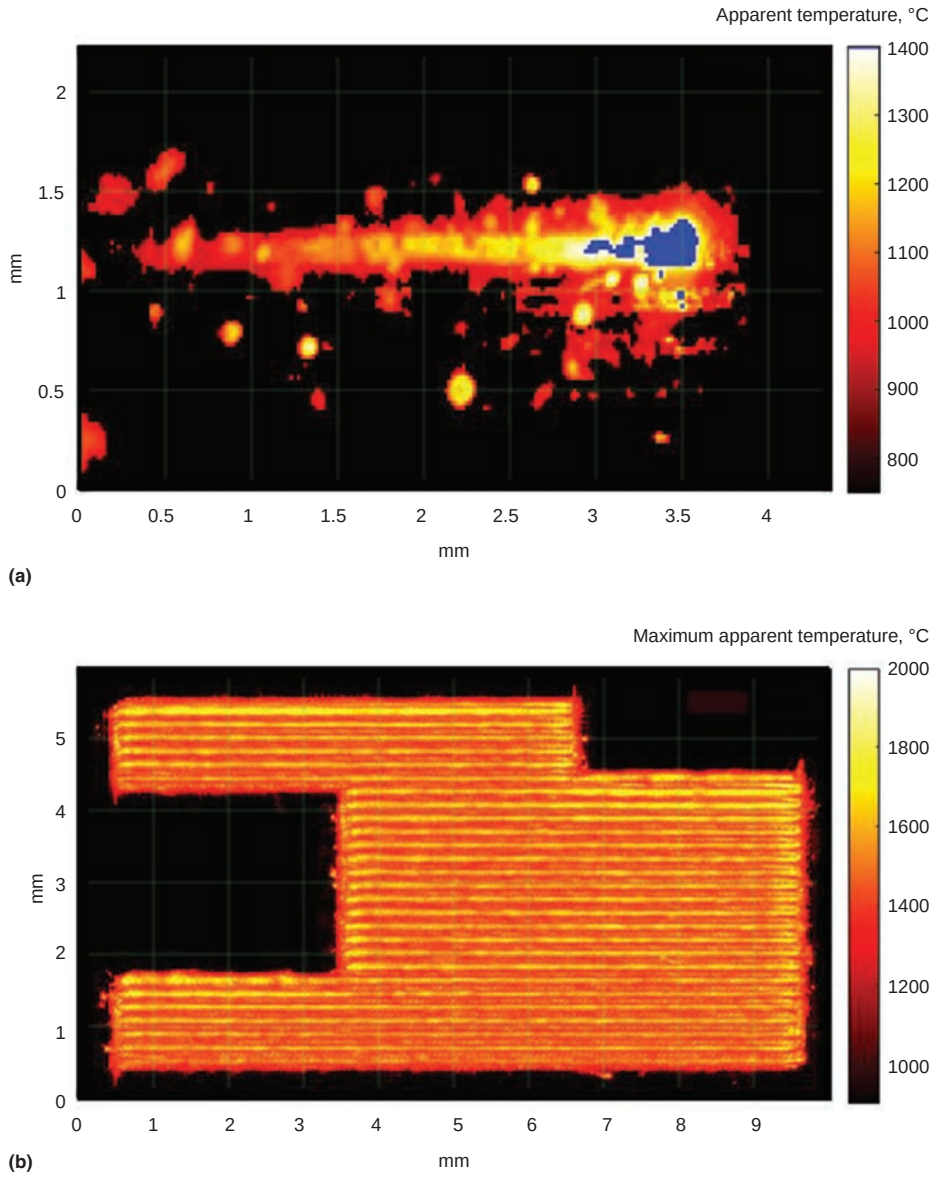

Fig. 1 (a) Melt-pool-scale thermal image from a high-speed, staring-configuration near-infrared camera (20 μm/pixel, 30,000 frames/s). (b) Part-scale thermal image measured via a high-speed coaxially mounted camera, with each image registered to part coordinates and superimposed (8 μm/pixel, 20,000 frames/s). Both images are based on laser powder-bed fusion of nickel superalloys.

Thermal Camera Types, Data Protocols, and Optics

The term *thermal camera* is generally attributed to those types that measure only infrared wavelengths. Any camera, including VIS spectrum or even color cameras, can be used as a thermal camera if its function enables some quantification of radiating thermal emission from an object that is then related to the object surface temperature. Because temperatures near the processing zone of metal AM are exceedingly high (more than 1000 °C, or 1830 °F), much of the thermal radiant emission is well within the VIS range. Also, as is shown in the section "Thermal Calibration" in this article, systems that measure a range of wavelengths (waveband) primarily consisting of shorter wavelengths such as VIS or near-infrared (NIR) have a relatively reduced measurable temperature range compared to

longer-wavelength systems such as midwave infrared (MWIR, or MIR) or long-wave infrared (LWIR). Altenburg et al. provided an in-depth investigation directly comparing three commercial off-the-shelf (COTS) thermal camera types (VIS; short-wave infrared, or SWIR; and MWIR) and noted some of the relative capabilities, advantages, and disadvantages when imaging DED processes (Ref 20).

Thermal cameras can primarily be categorized based on wavelength sensitivity spectrum and associated focal plane array (FPA) type, and acquisition speed (frame rate) and associated image data-transfer protocol. Table 1 summarizes the common FPA types and general notes on the respective COTS cameras. Apart from the camera, the material types and associated cost and performance of other optical components, such as lenses or windows, depend on the chosen wavelength range (Ref 21).

The cost of thermal cameras increases with acquisition speed (frame rate). Image and data acquisition can generally be categorized as onboard memory or data transmitting. Onboard-memory cameras directly transfer and store image data from the pixels to volatile memory placed physically near the chip within the camera body, often integrated as part of the chip hardware. These types of cameras can store tens of gigabytes of data and achieve greater than 100 kHz frame rates. For model/simulation development or underlying physical studies, onboard-memory cameras can provide the greatest spatial and temporal resolutions possible while acquiring gigabytes of image data in only a few seconds.

However, onboard-memory cameras typically cannot meet the data-storage requirements for monitoring/control, which requires many hours of an AM build. In these cases, cameras that transmit their data to a computer hard drive, network-attached storage, or external storage are used. However, the data-transmission protocol (e.g., GigE, Cameralink, CoaXPress, etc.; Ref 22) is the most common limiter to maximum image-acquisition rate. Mazzoleni et al. provided an exceptional literature review of many AM thermographic and other image-based measurements and compiled a pictograph comparing the related data-transfer protocols, frame rate, image sizes, and application for the measurements (Ref 3). Similar pictographs are provided elsewhere (Ref 23).

Table 1 Comparison of camera types, relative expense, and design considerations

Wavelength range	Common focal plane array types	Relative price	Notes
Visible spectrum (some near infrared)	Silicon (complementary metal oxide semiconductor, charge-coupled device)	$ to $$$	Many commercial options Lenses/optics relatively inexpensive Fewer thermally calibrated options Highest possible frame rates
Short-wave infrared	InGaAs	$$ to $$$	Few commercial high-speed options May use many common glass types (lower $)
Midwave infrared	HgCaTe, InSb	$$ to $$$	Cryo-cooled focal plane arrays Optics can be $$$ High-speed versions are $$$
Long-wave infrared	PbS, microbolometer	$ to $$	Can use silicon-based lenses/windows; relatively inexpensive Low integration time (i.e., motion blur)
	HgCaTe, strained layer superlattice	$$ to $$$	Cryo-cooled, higher-speed long-wave infrared options are $$$

Dual-Wavelength or Multispectral Thermography

Many AM researchers have explored use of dual- or multiwavelength thermographic methods for the purported advantage of not needing a priori knowledge of surface emissivity. Dual-wavelength systems have been employed coaxially (Ref 24, 25) or in staring configuration (Ref 26) and have been implemented as commercial products on AM systems. Additionally, several authors have investigated multispectral thermographic imaging in L-PBF (Ref 27, 28) or single-line hyperspectral on DED (Ref 29), primarily in research environments.

Compiling additional wavebands to a thermographic system inevitably increases complexity in the optical configuration and FPA design, thermal calibration, image interpretation or inference of temperature, results visualization, and data acquisition and data volume. Care should be taken because the purported advantages of multiwavelength thermometry also involve potential drawbacks. Multiwavelength systems require some assumption about the wavelength dependence of measured surface emissivity; either it is not dependent (i.e., graybody), or it follows some presumed wavelength-dependent function. Erroneous assumptions on this wavelength dependence can result in higher measured temperature errors compared to a single-wavelength or single-band system, which uses a single, non-wavelength-dependent emissivity value. A seminal paper by Coates et al. explored the potential for measurement error in dual- or multiwavelength thermometry using classic algorithms (Ref 30). Vollmer and Möllmann's thermography book provides an excellent analysis on the relative accuracy of single- versus dual-band thermography (Ref 31).

Metrological Basis of Thermography

Users of any measurement system must understand some of the underlying physical principles of that system. The formulas in this section may appear in various forms in literature or technical guides that accompany a purchased COTS camera. Although understanding all physical principles of these formulas is not entirely necessary, it is worthwhile to understand what assumptions precede their definitions and define their mutual relationships. Many radiometric terms are redundant, confusing, and often used improperly; users generally do not need to worry about the difference between terms such as *spectral radiance*, *exitance*, *irradiance*, *flux*, and so on. It is usually enough to understand that these radiance-based terms are all typically linearly related (e.g., if radiance doubles, then exitance, flux, irradiance, and so on double as well).

From Planck's Law to the Measurement Equation

The fundamental physical model for relating thermally radiating energy to surface temperature is provided via Planck's law, which relates the amount of radiating power, L, per unit surface area over a finite solid angle and at a specific wavelength of a perfect emitter (e.g., blackbody) to its temperature, T:

$$L(\lambda, T) \equiv \frac{c_{1L}}{\lambda^5(\exp(c_2/\lambda T) - 1)} \quad \text{(Eq 1)}$$

Here, $c_{1L} = 1.191{,}042{,}972 \times 10^{-16}\ \mathrm{W \cdot m^2 \cdot sr^{-1}}$ and $c_2 = 1.438{,}776{,}877 \times 10^{-2}\ \mathrm{m \cdot K}$ are the first and second radiation constants for spectral radiance, respectively, in SI units (Ref 32, 33). If wavelength is given in units of μm and emitting area in units of $\mathrm{m^2}$, it is sometimes convenient to use $c_{1L} = 1.191{,}042{,}972 \times 10^8\ \mathrm{W \cdot \mu m^4 \cdot m^{-2} \cdot sr^{-1}}$ and $c_2 = 1.438{,}776{,}877 \times 10^4\ \mathrm{\mu m \cdot K}$ (Ref 34). These constants are based on $c_{1L} = 2hc^2$ and $c_2 = hc/k_B$, where h is the Planck's constant, c is the speed of light, and k_B is the Boltzmann constant.

Wien's approximation is applicable to Planck's law for relatively short wavelengths and high temperatures, or $\lambda T < 3000\ \mathrm{\mu m \cdot K}$ (Ref 34, 35). Wien's has the added advantage that it is algebraically invertible and therefore commonly used in analytical approaches to system design, uncertainty analysis, and so on:

$$L^{\mathrm{Wien}}(\lambda, T) = \frac{c_{1L}}{\lambda^5 \exp(c_2/(\lambda T))} \quad \text{(Eq 2)}$$

Each pixel on a thermal camera outputs a signal that is related to the amount of energy

radiated by a surface and received by the pixel. In a real system, that radiating energy is reduced in magnitude by some real surface emissivity, $\varepsilon(\lambda, T)$ (unitless), and restricted in wavelength by some spectral responsivity, $r(\lambda)$ (unitless), of the camera. Spectral responsivity, $r(\lambda)$, includes transmission or reflection of all optical components within the optical path to the detector but is primarily defined by the spectral sensitivity of the FPA, the spectral transmission of the optics, and any spectral filter used. The radiated energy is further reduced by some finite amount, $A\Omega$ ($m^2 \cdot sr$), where $A\Omega$ is called the optical entendue, throughput, or optical extent and is related to the collection angle of the optics (Ref 36, 37), which is typically constant for a thermographic system. For a linear camera (see the section "Detector Linearity and Dynamic Range" in this article), the signal S is proportional to the received radiant energy (received radiant power integrated over the set integration time, t_{int}), scaled by $r(\lambda)$ and $\varepsilon(\lambda, T)$, and integrated over wavelength λ:

$$S(T) \propto \int_0^\infty \varepsilon(\lambda, T) r(\lambda) L(\lambda, T) d\lambda \quad \text{(Eq 3)}$$

If the bandpass of $r(\lambda)$ is relatively narrow, such that $\Delta\lambda$ is less than λ_0, the system may be called monochromatic. In that case, $r(\lambda) \approx 1$ and the integration in Eq 3 is unnecessary, resulting in $S \propto L(\lambda_0, T)$ in Eq 1. Care should be taken, however, because this is only applicable to monochromatic systems.

Multiple factors contribute to the proportionality coefficient in Eq 3, primarily associated with the lens optics and FPA. Holst (Ref 38) provides such a camera model, given in Eq 4. The equation shows that the detector signal is related to pixel area, A_D; system f-number, F_∞; and system magnification, M_{optics}:

$$\alpha \propto \frac{A_D t_{int}}{F_\infty^2 \left(1 + M_{optics}\right)^2} \quad \text{(Eq 4)}$$

Note that Eq 4 is an approximation assuming relatively high F_∞ and M_{optics} of less than 1; it is provided here to demonstrate the relative effect of these factors on camera signal. Equations 1 to 3 show how real radiant energy from a surface is related to the measured camera signal. Often, the real surface emissivity (as well as its spectral and temperature dependence) is unknown or can effectively be given a constant value of effective emissivity, ε_{eff}. The emitted radiant energy, scaled by this effective emissivity, can be equated to an apparent temperature, T_{app} (also known as radiance temperature, brightness temperature, or blackbody equivalent temperature), which is the temperature of an equivalent radiating source if its $\varepsilon_{eff} = 1$ (i.e., a blackbody). Note that both sides of Eq 5 are similar to the right side of Eq 3, meaning both sides are proportional to the camera signal:

$$\int_0^\infty r(\lambda) L\left(\lambda, T_{app}\right) d\lambda = \varepsilon_{eff} \int_0^\infty r(\lambda) L(\lambda, T_{surf}) d\lambda \quad \text{(Eq 5)}$$

If a user knows most of the variables in Eq 5, any unknown variable can be solved for by numeric integration and a minimization algorithm (Ref 39). An example online calculator is provided in Ref 40. Much of the COTS thermographic software uses something similar to Eq 5 or 6 to convert between measured signal, apparent temperature, and emissivity-corrected temperature nominally equivalent to the surface temperature, T_{surf}, absent any significant measurement error. In a different form, both sides of Eq 5 can be represented by the same temperature-dependent function, $F(T)$, called the calibration function:

$$S_{meas} = F\left(T_{app}\right) = \varepsilon_{eff} F(T_{surf}) \quad \text{(Eq 6)}$$

Equations 5 and 6 are often presented with an additional factor added to the right side related to the reflected radiant energy stemming from the ambient environment at temperature, T_{amb}, or $(1 - \varepsilon_{eff}) F(T_{amb})$. In cases where measured temperatures are much higher than ambient ($T_{surf} >> T_{amb}$) and/or emissivity is relatively high, the reflection correction may be neglected. It is usually only considered when measuring temperatures at or near ambient and/or for exceedingly low effective emissivity. Measured temperatures are relatively high for most AM applications, and reflected ambient radiation can be ignored. However, for highly reflective materials or those with relatively high thermal conductivity or low melting points, such as aluminum or copper, this may not be the case.

Thermal Calibration

Thermal calibration refers to the process of creating a map, or function, relating pixel signal values to the temperature(s) of a known thermally radiating source. Most often, this radiating source is a calibration blackbody, which is a physical instrument designed to replicate as closely as possible the radiance output of a perfect emitter or blackbody according to Eq 1 (e.g., $\varepsilon \approx 1$). This measurement equates $S_{meas} = F(T_{bb})$, where T_{bb} is the known blackbody temperature, thereby defining the calibration function F in Eq 6.

Figure 2 gives examples of three different hypothetical calibration curves calculated using Eq 3 over three example NIR, SWIR, and MWIR wavebands. A power-law model in the form of $S \propto T^n$ was fit to each curve to demonstrate the effect on the exponent n. Wavelength ranges (bands) were chosen such that the three curves have similar maximum values at 2500 °C (4530 °F).

Note in Fig. 2 that the lower limit of the NIR curve is at a higher temperature than the

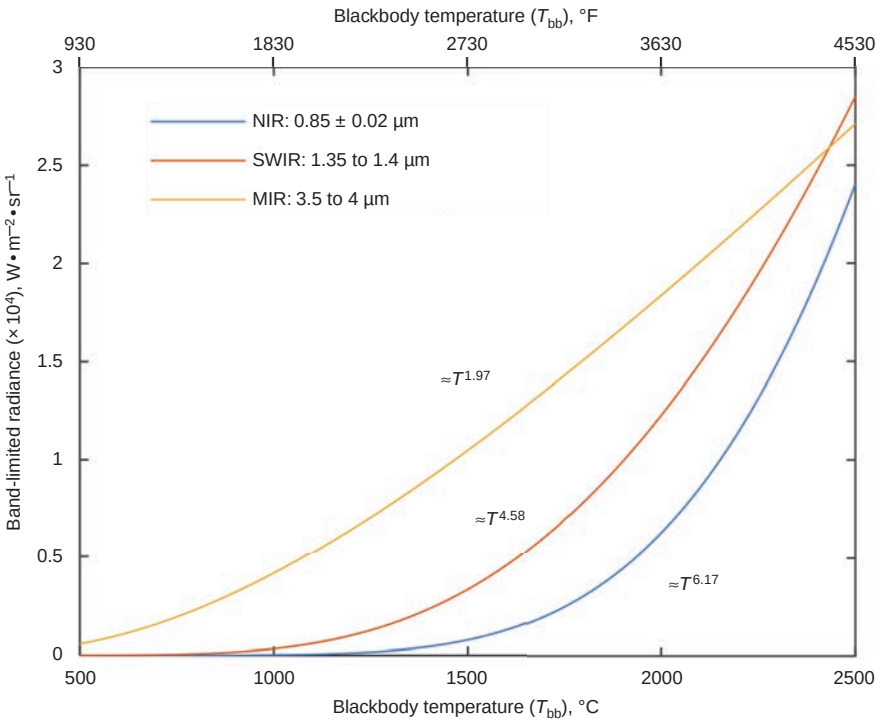

Fig. 2 Example calibration curves for hypothetical near-infrared (NIR), short-wave infrared (SWIR), and midwave infrared (MIR) systems based on Eq 3, with $r(\lambda) = 1$ between the band limits and $\varepsilon = 1$. A power-law calibration model, $S \propto T^n$, is fit to each curve, with exponent results shown.

SWIR or MIR examples, demonstrating that shorter-wavelength systems measure narrower temperature ranges, and vice versa. Similarly, longer SWIR and MIR wavelength ranges tend to have wider measurable temperature ranges, with the trade-off of lower sensitivity (i.e., change in signal per change in temperature). In summary, the shape of the calibration curves, which is primarily influenced by the spectral response, $r(\lambda)$, greatly influences critical measurement parameters such as range, sensitivity, uncertainty, and so on.

Effect of Integration Time on Measured Temperature

Apart from spectral response or wavelength range, integration time is another critical measurement parameter. According to Eq 4, integration time effectively scales the curves in Fig. 2 by some constant. Figure 3 gives an example of the MIR curve in Fig. 2, scaled to an equivalent camera signal in digital levels (DLs) and scaled to a 2× longer and 0.5× shorter integration time. For example, at a signal value S = 2000 DL, the 2× longer integration time results in lower measured apparent temperature; the opposite is true for the 0.5× shorter integration time. This shows how longer integration times enable measurement of lower temperatures, and vice versa.

Changing the sensor gain scales the calibration curve similarly to integration time and is often used to help bring a thermal scene into the viewable dynamic range (see the section "Detector Linearity and Dynamic Range" in this article). Some camera control software may also employ automatic gain control, which automatically adjusts gain until the mean pixel values in the image are within a specified range. However, adjusting gain does not typically extend the measurable temperature range or signal-to-noise ratio.

To expand measurable range, some newer cameras enable an operation called high dynamic range (HDR) imaging, enhanced dynamic range imaging, or superframing, which applies different integration times to sequential image frames during video capture. Each different integration time requires its own calibration or should have calibrations scaled by the new integration time(s), similar to Eq 4. For high-speed applications such as melt pool monitoring, the object of interest may move between image frames, disabling superposition of different exposure frames to extend the measurable temperature range of the melt pool. For example, Fig. 4 shows three sequential HDR image frames of an L-PBF melt pool at 5, 20, and 100 μs integration times. The hotter portions of the melt pool and fast-moving spatter particles within the field of view (FOV) move between frames.

Apart from changing the measurable temperature range, integration time has a critical influence on other factors, namely maximum frame rate and motion blur. These are discussed in the section "Motion Blur" in this article. Overall, it is critical to identify the target thermal phenomenon to be measured, as well as its relative temperature range, to select an appropriate spectral range and/or integration time.

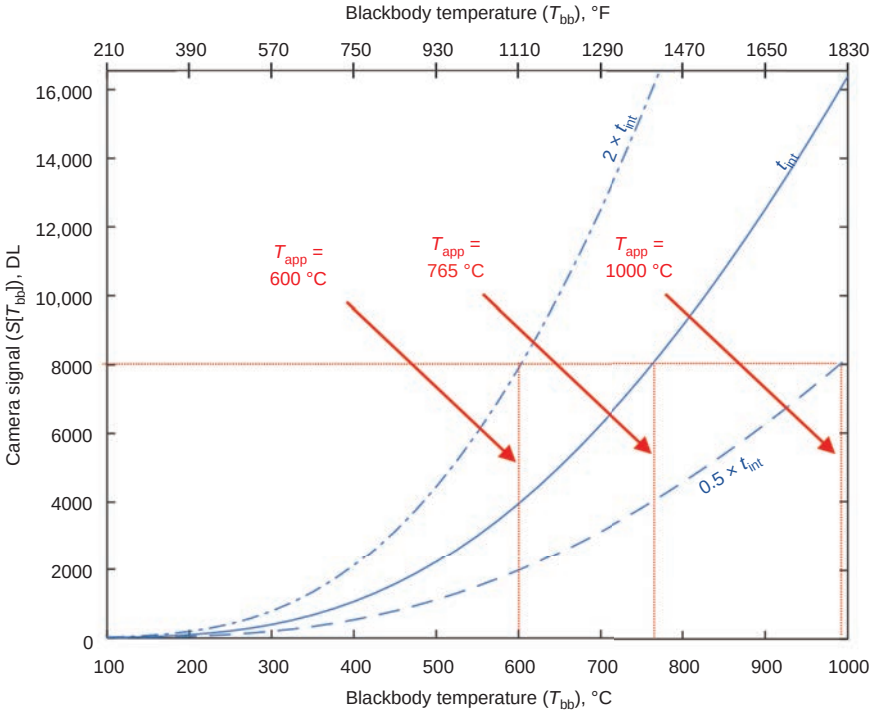

Fig. 3 Example midwave infrared calibration curve from Fig. 2, converted to camera signal values (digital levels, or DL) and scaled to longer (t_{int} = 2×) and shorter (t_{int} = 0.5×) integration times. Red lines show that a specific camera signal level equates to lower measured temperatures at a longer integration time. T_{app}, apparent temperature

Effect of Emissivity on Measured Temperature

Like integration time, emissivity has a direct effect on the relationship between the measured signal and the indicated temperature from the camera. Applying an ε_{eff} that most closely matches a real physical value results in a T_{surf} equal to the real, physical surface temperature. This is discussed in more detail in the section "Emissivity" in this article. Figure 5 demonstrates the relationship between T_{app}, T_{surf}, and ε_{eff} based on Eq 5 or 6 for the MIR example calibration in Fig. 2. As shown, lower emissivity results in a greater difference between T_{app} and T_{surf}.

As evident in Fig. 5, the error or change in ε_{eff} can drastically affect the measured temperature. In addition, ε_{eff} is assumed a constant value, where the real physical emissivity may be dependent on local temperature or surface condition (see the section "Emissivity" in this article). As shown in Fig. 2, the shape of these curves depends primarily on the wavelength choice. A change in camera signal (ΔS) stemming from an error in emissivity ($\Delta\varepsilon_{eff}$) results in a different temperature error (ΔT), depending on the shape of the curve. In other words, the sensitivity to errors depends greatly on the shape of the calibration curve. In general, shorter-wavelength systems are less sensitive to emissivity errors because they result in steeper signal-versus-temperature curves (i.e., higher $\Delta S/\Delta T$ or inversely lower $\Delta T/\Delta S$). Because an emissivity error ($\Delta\varepsilon_{eff}$) effectively results in a ΔS, the shorter-wavelength systems with lower $\Delta T/\Delta S$ are less affected by emissivity errors. This can be demonstrated analytically by manipulation of Eq 5 or 6 (Ref 31, 34, 35), as some AM thermographers have done (Ref 35).

Detector Linearity and Dynamic Range

As seen in Fig. 2, the wide temperature ranges exhibited in metals AM result in many decades of band-limited radiance and proportional camera signal response due to the exponential relationship with temperature. However, thermographic cameras have a finite range of indicated signal and measurable temperatures between a lower dark level (known as noise floor) and upper saturation, as seen in Fig. 6. This range is most often referred to as the dynamic range, although, similar to emissivity, this term is used

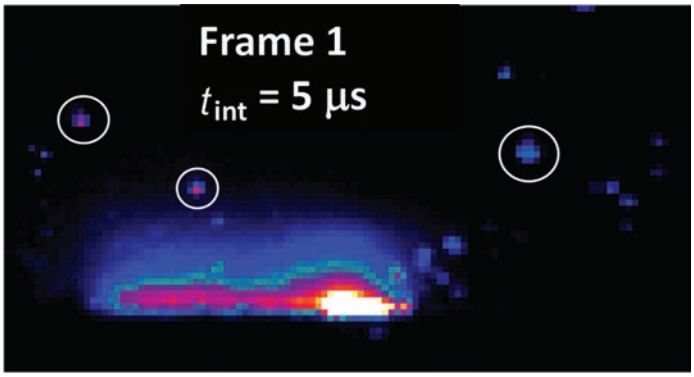

(a)

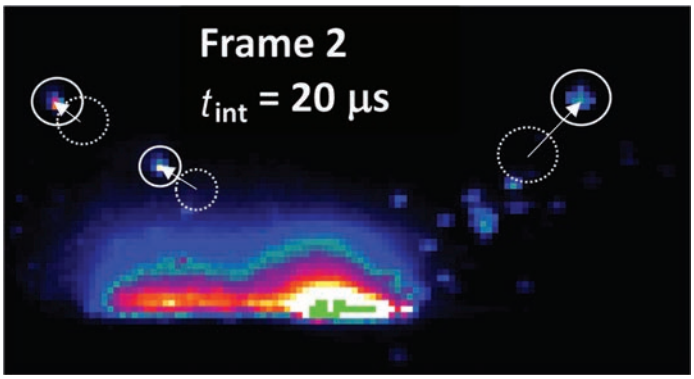

(b)

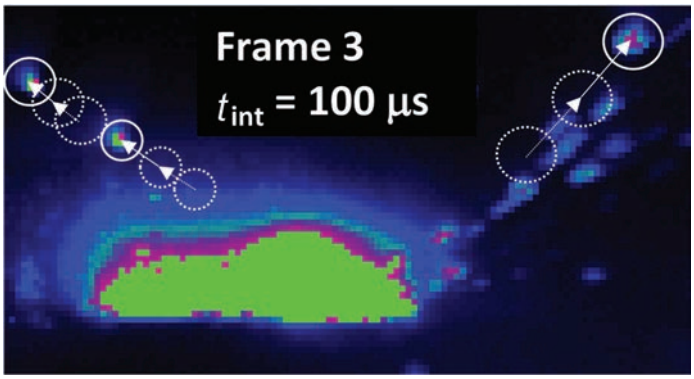

(c)

Fig. 4 Example high dynamic range image sequence at three different integration times (t_{int}). Images are 2500 frames/s, approximately 30 µm/pixel, capturing laser powder-bed fusion of a nickel superalloy. (a) to (c) Circles show locations of moving spatter particles between frames. The 100 µs image frame (c) also exhibits some elongated spatter particles due to increased motion blur. Pixel values are of camera signal (digital levels), and colormap range is set to arbitrary values, although green represents saturated pixels.

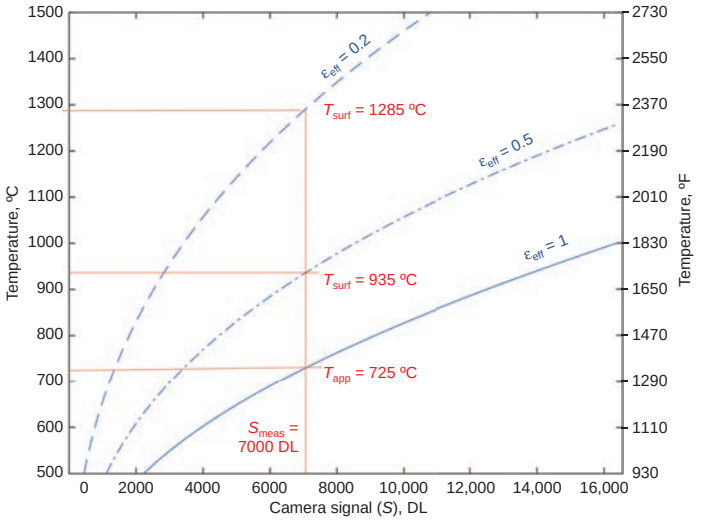

Fig. 5 Example midwave infrared calibration curve from Fig. 2 and 3, showing the effect of different effective emissivity (ε_{eff}) values on the emissivity-corrected surface temperature (T_{surf}). T_{app}, apparent temperature; S_{meas}, signal measurement; DL, digital level

colloquially to describe different concepts (Ref 41). Digital dynamic range describes how the measured signal is mapped to discrete digital levels (often 8, 12, or 14 bit). Between the dark and saturated signal levels, the actual signal response follows an S-shaped curve with respect to temperature or incident radiant flux on a pixel. In nearly every metal AM thermographic application, some part of the scene is below the measurable limit of the camera (e.g., dark level), and some part is saturated.

Thermal Calibration Sources and Techniques

Most AM researchers either rely on manufacturer-provided thermal calibration or forego any temperature-related measurand altogether. This is perfectly fine in many applications, as discussed in the section "Non-Temperature-Related Image Features" in this article. Systems not intended for temperature-related output still require other calibrations, such as spatial resolution (Ref 42) or testing for repeatability and reproducibility (Ref 43). In addition to achieving the same nominal temperatures of the target measurement, a thermal camera calibration source requires spatial uniformity as well as temporal stability. For temperatures above approximately 1000 °C (1830 °F), this generally requires specialized calibration sources not generally available to most users (Ref 44). However, several potential workarounds and characteristics of AM metals processing can be exploited.

First, relatively low emissivity of real metal surfaces equates to a higher measured temperature, T_{surf}, and thus measurable temperature range, as shown in Fig. 5. For example, an SWIR camera calibrated only to T_{app} = 1000 °C (1830 °F) using a COTS calibration blackbody and measuring an AM surface with assumed ε_{eff} = 0.221 has an upper measurement range of $T_{surf} \approx$ 1550 °C (2820 °F), which is well above the melting point of many AM alloys (Ref 45, 46). Although low emissivity has many deleterious consequences to thermal imaging accuracy, it does increase the measurable temperature range to higher temperatures.

Second, because the overall size of AM melt pools is relatively small, the total emitted radiant power is on the order of only several watts, despite high temperatures. Lane et al. showed that a 200 µm diameter blackbody source at approximately 2300 °C (4170 °F) (analogous to the size and temperature of an L-PBF melt pool) has the same radiant output as a COTS 1200 °C (2190 °F) blackbody source of 10 mm (0.4 in.) diameter (Ref 47). However, the calibration technique in that work is only applicable to single-point detectors, not a camera. Regardless, any calibration source designed for AM purposes would theoretically

require very little power to achieve the same radiant output as a melt pool, due to its relatively small size.

This fact can also result in a temperature measurement error called size-of-source error (SSE) if the calibration source is much larger or much smaller than the camera FOV or object being measured. This becomes challenging for smaller measured objects such as an AM melt pool. If the source is much larger, stray radiation from outside the FOV can enter the camera and erroneously increase the measured signal. If the source is much smaller, spatial resolution limits will attenuate the measured signal. Saunders and Edgar describe and compare three methods for measuring SSE (Ref 48). One of these methods, called the direct method, uses apertures of varying size in front of a uniform calibration source. Multiple examples in literature demonstrate the effect on temperature-measurement error stemming from SSE and too-large or too-small calibration sources (Ref 42, 49–51).

Finally, several methods have been attempted in AM research to directly relate measured camera signal to a reference temperature such as a thermocouple or the molten metal solidification, which can enable, alleviate, or altogether bypass thermal calibration via blackbody or another source. These methods are reviewed in the section "Measurements or Estimations of Metal AM Emissivity" in this article.

Emissivity

An oft-decried unknown in thermography, emissivity is required to convert a measured apparent temperature, T_{app}, to a temperature value closer to that of the real radiating surface, T_{surf}, in Eq 5 and 6. While physical emissivity values are complex, the effective emissivity concept is still intrinsically tied to a physical value. Therefore, understanding some general trends in how emissivity is related to material, wavelength, temperature, viewing angle, and so on can inform thermographic system design or results interpretation. The literature on metal emissivity values is numerous, but users should be aware when referencing these values: Values are often provided as the total hemispherical emissivity or emissivity coefficient (Ref 52), which is applicable to radiation heat transfer and the Stefan-Boltzmann law. Spectral-directional or normal-spectral emissivity is more applicable to thermographic measurements. In addition, measured values from different researchers or repeated measurements by the same often disagree by approximately 10% or more, despite careful measurement methods and system designs.

A comprehensive review of measured emissivity for AM metals is beyond the scope of this article. Touloukian and DeWitt (Ref 53) provide a quite comprehensive cumulation of metal emissivity values, and many more recent references exist (Ref 53–57). Based on reviews of these references and others, several general statements can be made regarding normal- or directional-spectral emissivity of metals:

- Emissivity decreases with wavelength, with a sharp decline in the VIS-SWIR spectrum followed by a gradual decline from SWIR to LWIR (Fig. 7).
- Emissivity is not highly sensitive to temperature, at least in the solid phase (this assumes no secondary effect such as oxidation, which can significantly increase emissivity).
- Emissivity can increase significantly with surface roughness, particularly in the vicinity of surface cavities (e.g., cavities in metal powder or a melt pool vapor depression).
- Emissivity is relatively insensitive to the view angle for rough or diffuse surfaces (e.g., powder) but highly sensitive to the view angle for shiny or specular surfaces (e.g., recently molten and solidified metal).

In general, measurement of high metal AM temperatures using the VIS-NIR spectrum has the advantage of higher emissivity, which brings the potential disadvantage of greater sensitivity to wavelength. Wavelength dependence on emissivity becomes more critical for wider-band spectral responsivity $r(\lambda)$, because the emissivity term in Eq 3 may no longer be pulled from the wavelength integral, as in Eq 5. Also note that the graybody assumption made in some ratio or dual-band methods worsens for measuring metals at shorter wavelengths. For high-magnification thermography, local effective emissivity may vary drastically based on the type of radiating surface, whether it is powder, solid metal, liquid metal, or incandescing metal vapor (Ref 44). Additionally, a cavity or depression, such as between powder particles or the commonly cited vapor depression in L-PBF, may effectively increase the local emissivity within that cavity (Ref 44, 58).

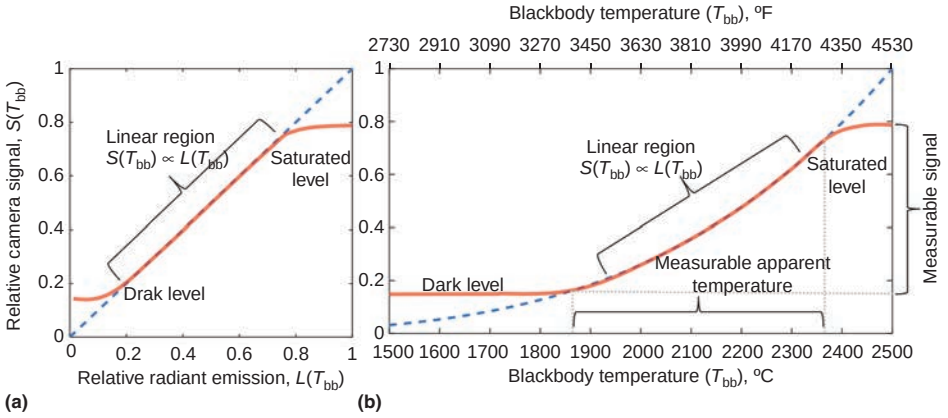

Fig. 6 Example of dark level, linear range, and saturation limits on measurable signal (S) with respect to (a) radiant emission (L) or (b) blackbody temperature (T_{bb}). The blue dotted line indicates the "perfect" linear camera model of Eq 3, and the red line reflects real physical limits of that model.

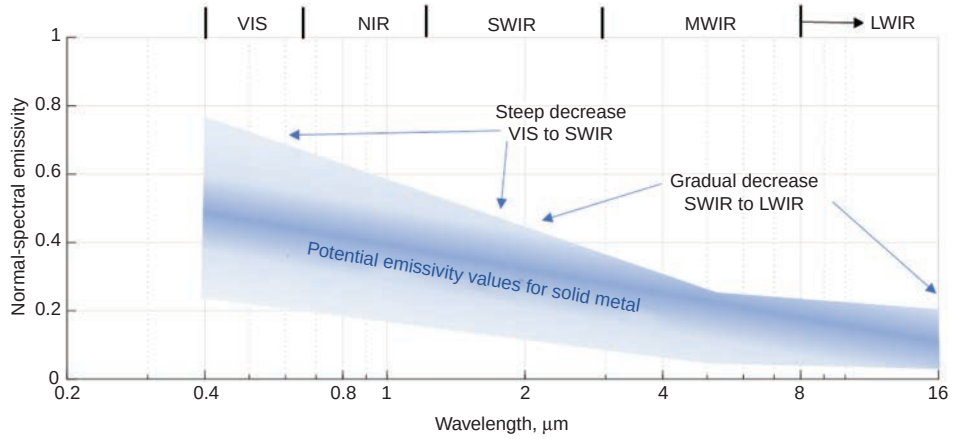

Fig. 7 General trend for normal-spectral emissivity of solid metals common in additive manufacturing (with relatively polished surface), based on a review of Ref 53 and multiple other sources. Note the logarithmic wavelength axis. VIS, visible; NIR, near infrared; SWIR, short-wave infrared; MWIR, midwave infrared; LWIR, long-wave infrared

Measurements or Estimations of Metal Additive Manufacturing Emissivity

In lieu of estimating emissivity, various methods for direct measurement using a thermal camera are possible; several have been attempted in AM research. Madding provided a concise summary of several generalized, practical approaches for measuring emissivity with a thermal camera (Ref 59). These were categorized as:

- *Reference emitter:* A known emissivity material, such as paint or a local blackbody-like cavity, is applied to the measured target.
- *Reference temperature:* A secondary measurement of the target temperature is made (e.g., with a thermocouple).
- *Two temperature:* The target is raised to different known temperatures, and emissivity is based on a ratio of the measured camera signals versus that of an equivalent blackbody.
- *Reflectivity:* Some method for measuring surface reflectivity is made, and emissivity is equated to $\varepsilon = 1 - \rho$ according to Kirchoff's law, where ρ is the reflectivity.

The AM thermography researchers have used various methods related to these technique categories to measure emissivity, including:

- *Reference temperature:* based on solidification (Ref 45, 46, 60–65)
- *Reference temperature:* based on thermocouple (Ref 25, 66–69)
- *Reference emitter:* fabricated blackbody cavity (Ref 70, 71)
- *Reflectivity techniques* (Ref 44, 72, 73)

Overall, it is valuable to estimate *a priori* the effect of an erroneous emissivity assumption on the measured temperature and to evaluate if this error warrants further efforts to measure emissivity and improve the assumption. In AM thermography, these measurement errors were included in measurement analysis by Boone et al. (Ref 74) and Kledwig et al. (Ref 75).

Special Considerations for Additive Manufacturing Thermographic Systems

Imaging Challenges

The metal AM process creates a challenging environment for thermography. The rapid melting of metals can cause image attenuation and associated evaporation, changes in the optical path distance, imager damage, extraneous light sources, and more. While some challenges are mitigable, others remain for thermographic measurements in the metal AM environment.

Reflected, Scattered, and Leaked Laser Light

A scanned and focused laser beam with power on the order of several hundred watts is applied in metals L-PBF and laser-based DED. Depending on the process parameters and material, 50% or more of the applied power may be reflected and scattered within the build chamber (Ref 76). As a result, safety engineering measures such as laser-blocking windows, shutters, or interlocks must be implemented if any modifications to the build chamber (especially the windows) are implemented with the thermography system introduction. In addition, because the imager may be focused on the melt pool region from which laser light is reflected, the imager must be protected from reflected laser light, which can damage the detector. The VIS and NIR detectors can also be sensitive to the laser wavelength; even a small percentage of scattered laser energy received by the detector may erroneously add to the apparent thermal emission of the melt pool. This may occur if a window or bandpass filter does not sufficiently attenuate the laser wavelength with many orders of magnitude optical density.

Additionally, excessive laser energy must not be absorbed as heat in any spectral filters or windows used to block the laser wavelength from the camera sensor, because this could alter spectral performance of the filter in the transmitting spectra. If reflective-type spectral filters are to be used, multiple reflections can occur between the filters and other optical component surfaces. This may result in light leakage and imaging artifacts. The efficacy of laser attenuation may be evaluated by defocusing the beam and scanning across a smooth, reflective surface. In this way, the surface is not significantly heated, but the laser light is reflected and scattered, with minimal (if any) signal detected by the camera, indicating likely adequate protection from laser damage or erroneous measurement. Additionally, modulating the defocused laser power and monitoring for a synchronous signal change in the imager can help isolate if the additional signal is from laser scattering or another asynchronous source.

Chamber Temperature and Pressure

The chamber temperature and process pressure may affect thermographic measurements in several ways:

- Compression or expansion of the chamber and seals may change the optical path distance from the detector to the measured surface.
- Changes in chamber temperature and pressure can distort windows and optics, as well as change the bulk optical properties of the gas in the chamber.
- Changes in chamber temperature can alter reflected ambient radiance, especially for low-temperature, long-wavelength applications (e.g., see the note following Eq 6).

Each of these effects is typically minor but can be significant under certain circumstances. To minimize temperature-measurement uncertainty, a thermal calibration should be conducted under conditions that are as similar as possible to the conditions at which thermography is to be performed. Similarly, one should ensure that dimensional accuracy and image sharpness are maintained under process conditions.

Optical Path Contamination

Metal AM processes may result in a variety of by-products, including metal vapor, condensate, reactive impurities, hot ejecta, and powder particles, which can contaminate windows, optics, and gas within the process chamber. Such contamination can change calibration over time, reduce image dimensional accuracy, and result in image artifacts that change with the level of contamination. Process by-product contamination suspended in the chamber gas flow may result in similar thermographic performance degradation. For L-PBF or laser-based DED, the primary prevention of optical path contamination is the expedient removal of process by-products from the build chamber through controlled gas flow across the laser processing area and often across the laser optics as well, although this engineering solution does not fully mitigate the contamination. Metallization can affect thermographic windows for E-PBF or processes occurring in vacuum, contributing to variable and significant transmission loss. Various researchers and commercial E-PBF systems have employed shutter mechanisms (Ref 70) and film-protected windows (Ref 77) or have measured and compensated for this transmission loss (Ref 78). Thus, in addition to conducting calibrations at similar conditions to the AM processing, users should confirm image sharpness, dimensional accuracy, and thermal calibration before and after activities that may result in significant contamination.

Motion Blur

Motion blur occurs when any detectable object within the FOV moves relative to the FOV during the integration period of an acquired image frame. Both translational and/or oscillatory motion (i.e., change in shape) can induce motion blur. Generally, any rapid change in surface temperature or thermal scene at a fixed point in the FOV may incur a motion blur effect if it is fast relative to the integration period. In metal AM, particularly PBF, the primary source for motion blur stems from the controlled scanning strategy, which, for staring-configuration cameras, observes the melt pool or heated region translating relative to the FOV. For high-magnification systems, molten melt pools also exhibit oscillations in size and shape due to dynamic residual heat effects nominally concurrent with scan

strategy harmonics (Ref 45, 79). Additionally, complex oscillation modes occur on the molten liquid surface (Ref 80, 81). Staring configurations may therefore incur motion blur from all three types of melt pool motion, while coaxial configurations have more complex motion blur effects. The heat source and resulting thermal field are nominally stationary in the FOV, while the underlying powder or substrate move with respect to the FOV based on the scan speed of the laser or heat source. For high-temperature coaxial configurations that primarily observe the molten portion of the melt pool, abrupt changes in melt pool size, shape, or temperature, as well as particularly hot and fast-moving spatter/ejecta, may incur motion blur. If relatively lower temperatures are observed in the powder or vicinity adjacent to the melt pool, these objects may appear to incur motion blur based on the relative scan speed.

In any case, motion blur can lead to significant uncertainties in temperature measurement. Therefore, the shortest integration time that results in the desired dynamic range or measured temperature range should be used (see the section "Effect of Integration Time on Measured Temperature" in this article). However, optical tomography (OT) (Ref 82), a commercial monitoring product for L-PBF, incorporates motion blur as part of its design. By varying integration time, the staring thermal camera of the OT system observes and superimposes phenomena such as surface heat accumulation or plume and spatter. Although not quantitative thermography, these image features are anticipated to be good enough analogs for identifying fabrication defects or heterogeneity and are incorporated in in situ process quality-control methods (see the section "Thermographic Setups in AM Research" in this article).

Unfortunately, motion blur cannot be eliminated and may not always be evaluated or quantified. Furthermore, methods to compensate motion blur via image processing (e.g., deconvolution of a motion blur kernel) are generally impractical for in situ AM thermal scenes due to the complex motions described previously. However, motion blur may be considered negligible if the blur length, δ_{blur}, is less than the equivalent pixel size, δ_{pixel}, on the object plane, or $\delta_{blur} < \delta_{pixel}$. For translational motion, the blur length may be estimated as $\delta_{blur} = vt_{int}$, where v is the object motion speed, and t_{int} the integration time. Estimation is more complex for oscillatory motion, particularly if the oscillations are not at a single frequency. However, assuming a pure sinusoidal motion with amplitude a and frequency ω (in rad/s), if t_{int} is less than $2\pi/\omega$, the blur distance then depends on the instantaneous speed of the object, with a maximum $\max(\delta_{blur}) = a\omega t_{int}$. For high frequencies, where t_{int} is greater than $2\pi/\omega$, the blur length may be estimated as $\delta_{blur} = 2a$ and compared to δ_{pixel}. These calculations may help determine when motion blur is negligible. However, if it is found to be non-negligible, effects of the motion blur on quantitative temperature measurement may be very complex. The authors are unaware of any standard or generalized methods for motion blur compensation or temperature uncertainty estimation.

Stray Light and Blooming

As mentioned previously, melt pool temperatures can exceed the metal boiling point (>3000 °C, or 5430 °F) (Ref 83). Due to the exponential nature of Eq 1, this can result in many orders of magnitude difference in radiant emission between the areas outside and inside the melt pool. This high-intensity light from the hottest part of the melt pool can locally increase the measured signal on pixels adjacent to the hot spot by stray light generation and/or an effect called detector blooming. Stray light may stem from many sources. In the case of high-intensity bright spots in an image, stray light is generated from imperfections in the focusing optics, causing a portion of the imaged light to diverge from its ideal path. Because light from the hot spot is intense, a small amount of scattering may generate a significant increase in the thermographic signal near the hot spot. An effect of stray light known as lens flare is illustrated in Fig. 8, which shows a vertical and horizontal cross pattern centered on the melt pool hot spot.

Blooming occurs when the highly intense bright spot is transmitted to the detector, overfilling the pixel electron wells (i.e., saturating), which may then leak additional charge into adjacent pixels and increase their measured signal. The effects of stray light and blooming may be estimated by creating a light source designed with approximately the same size and radiant output as the hot spot, focusing on this source, and observing the relative amount of signal gain in adjacent pixels (Ref 44).

Plume Effects

As described previously, metal AM generates by-products that can affect the thermographic camera optical path. The effects of such by-products are much more significant when measuring at melt pool scales. The metal vapor generated at the laser hot spot is expelled at high temperatures in a jet by vapor recoil and can incandesce with observable radiant emission. It then rapidly cools and forms nanoscale condensate that may also include gas impurities. This condensate is often referred to as the plume (Ref 84). The nanoscale condensate, which can scatter or absorb the laser energy, may also be reheated by the laser and add to the apparent radiant emission of the melt pool surface, biasing the registered temperature to higher values, as illustrated in Fig. 8. Thermal emission from the plume may also reflect from the surface and further increase the apparent temperature of the melt pool and surrounding area (Fig. 8). Furthermore, the nanoscale by-products may scatter radiated emission from the melt pool or shift the relative refractive index of the gas, which can attenuate the emission or distort the apparent shape. Microscale ejecta may result in similar effects to the nanoscale by-products but in localized, discrete events.

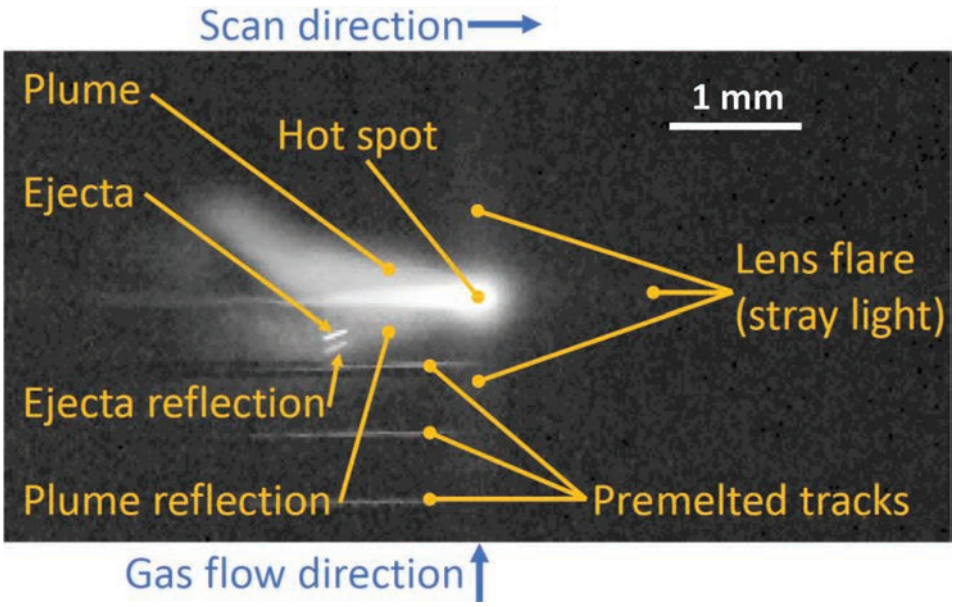

Fig. 8 Example of a near-infrared (0.85 ± 0.2 nm) staring-configuration thermographic image of a laser powder-bed fusion melt pool on a bare metal plate (20 μm/pixel). The image is gamma adjusted to accentuate lower signal values. A crosslike lens flare pattern is observable and centered on the melt pool hot spot. The bright plume obscures the melt pool, and both plume and particle ejecta create reflections on the substrate.

The geometric and spectral properties of the plume depend on the material, process power, scan speed, spot size, and gas flow speed and direction (Ref 44, 85, 86), which makes the plume effects on thermography highly variable. Radiance from the plume of process by-products can be the largest temperature-measurement uncertainty component (Ref 44); mitigation of such effects remains a topic that requires further research.

Non-Temperature-Related Image Features

Most process monitoring or control objectives, particularly for AM, may not actually necessitate direct relation to physical temperatures. Real surface temperature values are often necessary for model validation or fundamental physical studies (see the section "Thermographic Setups in AM Research" in this article), whereas monitoring and control operations primarily rely on quantifying the general stability or variability of one or more monitored parameters. However, thermal calibration is necessary for parameters such as thermal gradient, cooling rates, or maximum temperature (Ref 87). For machine-vision systems, including thermography, parameters extracted from an image or video are often referred to as image features.

The most common approach to deriving image features from AM melt pool monitoring is to first threshold or binarize the thermal images (e.g., set all pixel values above a certain value to 1 and all below that value to 0), then calculate a variety of univariate properties on the binarized image. For example, a commonly cited image feature taken from binarized melt pool images is the melt pool area, seen on commercial L-PBF melt-pool-monitoring products (Ref 88, 89) and widely used among researchers (Ref 90–92). Similarly, various researchers have explored separating (i.e., segmenting) parts of thermal images attributed to the incandescing plume or spatter particles and quantifying parameters such as shape or particle count as a potential analog to fabrication quality (Ref 86, 93–96). Another commonly referenced image feature called time above temperature or time above threshold has been demonstrated for staring camera systems (Ref 97–99).

A more recent AM thermography trend is the extraction of image features using machine-learning (ML) methods (Ref 16, 100, 101). While the variety and utility of ML methods for AM image-processing and process-monitoring data analytics are beyond the scope of this article, these methods generally do not require thermographic image data to be related to physical temperatures.

Coaxial System Design Challenges

Coaxial melt pool imaging provides several advantages to staring-configuration cameras, with the added cost of complexity in the optical system design. The coaxial optical design complexities largely stem from the needs of the two separate optical systems: one that forms a consistent, focused, high-energy laser spot scanned over a flat area; and one optimized for imaging quality at a wavelength other than that of the laser. The motion axes that position the laser spot are often rectilinear for DED systems, so the optical path length for both laser and camera can be constant or make use of an infinite-conjugate lens system. In L-PBF systems, which steer the laser beam using rotating mirrors (e.g., a galvanometer, or galvo, scanner), the variable path length between the rotating mirrors and the flat powder bed requires flat-field correction, which employs either a stationary *f*-theta lens below the galvo or a dynamically positioned focusing lens between the laser collimator and galvo mirrors. The *F*-theta lenses are complex, multielement optical assemblies specially optimized for flat-field correction of a laser.

Few literature examples include design details of coaxial camera systems for use in conjunction with an *f*-theta galvo system (Ref 25, 102–104). Certain aspects of *f*-theta galvo systems lead to difficulty in designing a thermographic, coaxial imaging system around them, including:

- Chromatic or monochromatic (e.g., spherical, astigmatism, etc.) aberrations, dependent on galvo position
- Variable spectral transmission of the *f*-theta lens, galvo mirror coatings, and/or beam splitters (Fig. 9)
- Relatively high *f*-number of laser-galvo systems reduces light collection and camera sensitivity (Eq 4)

Fewer coaxial imaging systems are designed around a customized dynamic focusing lens (Ref 105–107). While these custom lenses may be designed to alleviate some of the chromatic or monochromatic aberrations mentioned in the first two bulleted points in the aforementioned list, they are still limited to relatively high *f*-numbers, relegating them sensitive to only relatively higher temperatures (>1000 °C, or 1830 °F).

REFERENCES

1. R. Komanduri and Z.B. Hou, A Review of the Experimental Techniques for the Measurement of Heat and Temperatures Generated in Some Manufacturing Processes and Tribology, *Tribol. Int.*, Vol 34, 2001, p 653–682
2. S. Berumen, F. Bechmann, S. Lindner, J.-P. Kruth, and T. Craeghs, Quality Control of Laser- and Powder Bed-Based Additive Manufacturing (AM) Technologies, *Phys. Proced.*, Vol 5 (Part B), 2010, p 617–622
3. L. Mazzoleni, A.G. Demir, L. Caprio, M. Pacher, and B. Previtali, Real-Time Observation of Melt Pool in Selective Laser Melting: Spatial, Temporal, and Wavelength Resolution Criteria, *IEEE Trans. Instrum. Meas.*, Vol 69 (No. 4), 2020, p 1179–1190
4. S.K. Everton, M. Hirsch, P. Stravroulakis, R.K. Leach, and A.T. Clare, Review of In-Situ Process Monitoring and In-Situ Metrology for Metal Additive Manufacturing, *Mater. Des.*, Vol 95, 2016, p 431–445
5. M. Grasso and B.M. Colosimo, Process Defects and In Situ Monitoring Methods in Metal Powder Bed Fusion: A Review, *Meas. Sci. Technol.*, Vol 28 (No. 4), 2017, p 044005
6. M. Grasso, A. Remani, A. Dickins, B.M. Colosimo, and R.K. Leach, In-Situ Measurement and Monitoring Methods for Metal Powder Bed Fusion: An Updated Review, *Meas. Sci. Technol.*, Vol 32 (No. 11), 2021, p 112001

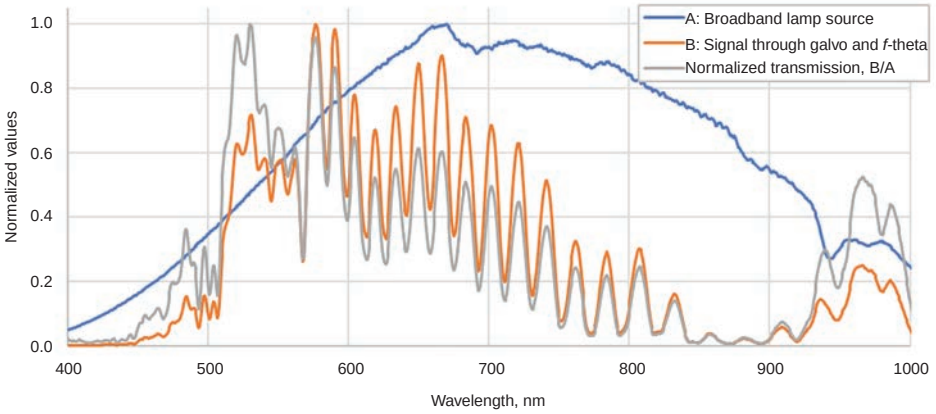

Fig. 9 Relative spectral transmission through the *f*-theta, galvo mirrors, and melt-pool-monitoring beam splitter of a commercial laser powder-bed fusion machine

7. D. Li, R. Liu, and X. Zhao, Overview of In-Situ Temperature Measurement for Metallic Additive Manufacturing: How and Then What, *Proc. Solid Freeform Fabrication Symposium*, University of Texas at Austin (Austin, TX), 2019, http://dx.doi.org/10.26153/tsw/17384
8. M. Mani, B.M. Lane, M.A. Donmez, S.C. Feng, and S.P. Moylan, A Review on Measurement Science Needs for Real-Time Control of Additive Manufacturing Metal Powder Bed Fusion Processes, *Int. J. Prod. Res.*, Vol 5, 2016, p 1–19
9. R. McCann, M.A. Obeidi, C. Hughes, É. McCarthy, D.S. Egan, R.K. Vijayaraghavan, A.M. Joshi, V. Acinas Garzon, D.P. Dowling, P.J. McNally, and D. Brabazon, In-Situ Sensing, Process Monitoring and Machine Control in Laser Powder Bed Fusion: *A Review, Addit. Manuf.*, Vol 45, 2021, p 102058
10. E. Reutzel and A. Nassar, A Survey of Sensing and Control Systems for Machine and Process Monitoring of Directed-Energy, Metal-Based Additive Manufacturing, *Rapid Prototyp. J.*, Vol 21 (No. 2), 2015, p 159–167
11. Z. Yan, W. Liu, Z. Tang, X. Liu, N. Zhang, M. Li, and H. Zhang, Review on Thermal Analysis in Laser-Based Additive Manufacturing, *Opt. Laser Technol.*, Vol 106, 2018, p 427–441
12. K.M. Taminger, C.S. Domack, J.N. Zalameda, B.L. Taminger, R.A. Hafley, and E.R. Burke, In-Process Thermal Imaging of the Electron Beam Freeform Fabrication Process, *Thermosense: Thermal Infrared Applications XXXVIII*, SPIE, 2016, p 986102, doi:10.1117/12.2222439
13. J.N. Zalameda, E.R. Burke, R.A. Hafley, K.M. Taminger, C.S. Domack, A. Brewer, and R.E. Martin, Thermal Imaging for Assessment of Electron-Beam Freeform Fabrication (EBF3) Additive Manufacturing Deposits, *Proc. SPIE*, Vol 87050M, International Society for Optics and Photonics, 2013, p 87050M
14. R.B. Dinwiddie, L.J. Love, and J.C. Rowe, Real-Time Process Monitoring and Temperature Mapping of a 3D Polymer Printing Process, *Proc. SPIE*, Vol 87050L, 2013, p 87050L–9, http://dx.doi.org/10.1117/12.1518454
15. S. Afazov, A. Roberts, L. Wright, P. Jadhav, A. Holloway, H. Basoalto, K. Milne, and N. Brierley, Metal Powder Bed Fusion Process Chains: An Overview of Modelling Techniques, *Prog. Addit. Manuf.*, 2021, doi:10.1007/s40964-021-00230-1
16. T. DebRoy, T. Mukherjee, H.L. Wei, J. W. Elmer, and J.O. Milewski, Metallurgy, Mechanistic Models and Machine Learning in Metal Printing, *Nat. Rev. Mater.*, Vol 6 (No. 1), 2021, p 48–68
17. W.E. King, A.T. Anderson, R.M. Ferencz, N.E. Hodge, C. Kamath, S.A. Khairallah, and A.M. Rubenchik, Laser Powder Bed Fusion Additive Manufacturing of Metals; Physics, Computational, and Materials Challenges, *Appl. Phys. Rev.*, Vol 2 (No. 4), 2015, p 041304
18. B. Soundararajan, D. Sofia, D. Barletta, and M. Poletto, Review on Modeling Techniques for Powder Bed Fusion Processes Based on Physical Principles, *Addit. Manuf.*, Vol 47, 2021, p 102336
19. H.L. Wei, T. Mukherjee, W. Zhang, J.S. Zuback, G.L. Knapp, A. De, and T. DebRoy, Mechanistic Models for Additive Manufacturing of Metallic Components, *Prog. Mater. Sci.*, 2020, p 100703
20. S.J. Altenburg, A. Straße, A. Gumenyuk, and C. Maierhofer, In-Situ Monitoring of a Laser Metal Deposition (LMD) Process: Comparison of MWIR, SWIR and High-Speed NIR Thermography, *Quant. InfraRed Thermogr. J.*, 2020, p 1–18
21. "The Correct Material for Infrared (IR) Applications," Edmund Optics, https://www.edmundoptics.com/knowledge-center/application-notes/optics/the-correct-material-for-infrared-applications/, accessed Feb 4, 2022
22. "Vision Standards," Association for Advancing Automation (A3), https://www.automate.org/a3-content/vision-standards, accessed Jan 9, 2022
23. "Interfaces for Machine Vision," Teledyne FLIR, 2020, https://www.flir.com/discover/iis/machine-vision/interfaces-for-machine-vision/, accessed Dec 29, 2021
24. J. Craig, S.M. Kelly, T. Reutzel, and O. Grylls, "Multi-Sensing Process Monitoring and Control of Directed Energy AM Processes" (Orlando, FL), ASM International, 2014
25. P.A. Hooper, Melt Pool Temperature and Cooling Rates in Laser Powder Bed Fusion, *Addit. Manuf.*, Vol 22, 2018, p 548–559
26. J.A. Mitchell, T.A. Ivanoff, D. Dagel, J. D. Madison, and B. Jared, Linking Pyrometry to Porosity in Additively Manufactured Metals, *Addit. Manuf.*, Vol 31, 2020, p 100946
27. N.P. Calta, G. Guss, S. Wu, S. Ly, D. Deane, M.F. Crumb, and M.J. Matthews, High Speed Hyperspectral Thermal Imaging of the Melt Pool Dynamics during Metal Additive Manufacturing, *2017 Conference on Lasers and Electro-Optics (CLEO)*, 2017, p 1, 2
28. N. Gerdes, C. Hoff, J. Hermsdorf, S. Kaierle, and L. Overmeyer, Snapshot Hyperspectral Imaging for Quality Assurance in Laser Powder Bed Fusion, *Proced. CIRP*, Vol 94, 2020, p 25–28
29. W. Devesse, D. De Baere, and P. Guillaume, High Resolution Temperature Measurement of Liquid Stainless Steel Using Hyperspectral Imaging, *Sensors*, Vol 17 (No. 1), 2017, p 91
30. P.B. Coates, Multi-Wavelength Pyrometry, *Metrologia*, Vol 17 (No. 3), 1981, p 103
31. M. Vollmer and K.-P. Möllmann, *Infrared Thermal Imaging: Fundamentals, Research and Applications*, 2nd ed., Wiley-VCH, Weinheim, Germany, 2018
32. E. Tiesinga, P.J. Mohr, D.B. Newell, and B.N. Taylor, The 2018 CODATA Recommended Values of the Fundamental Physical Constants (Web Version 8.1), *Fundamental Physical Constants from NIST*, National Institute of Standards and Technology, 2019, http://physics.nist.gov/cuu/Constants/index.html, accessed Nov 9, 2021
33. E. Tiesinga, P.J. Mohr, D.B. Newell, and B.N. Taylor, CODATA Recommended Values of the Fundamental Physical Constants: 2018, *J. Phys. Chem. Ref. Data*, Vol 50 (No. 3), AIP Publishing LLC for the National Institute of Standards and Technology, 2021, p 033105
34. D.P. DeWitt and G.D. Nutter, *Theory and Practice of Radiation Thermometry*, Wiley Online Library, 1988
35. P. Saunders, *Radiation Thermometry: Fundamentals and Applications in the Petrochemical Industry*, SPIE Press, 2007
36. "Light Collection and Optical System Throughput," MKS|Newport, https://www.newport.com/t/light-collection-and-systems-throughput, accessed Nov 24, 2021
37. Z.M. Zhang, B.K. Tsai, and G. Machin, *Radiometric Temperature Measurements: I. Fundamentals*, Academic Press, 2009
38. G.C. Holst, *Testing and Evaluation of Infrared Imaging Systems*, JCD Publishing, Winter Park, FL; SPIE Press, Bellingham, WA, 2008
39. E.P. Whitenton, "High-Speed Dual-Spectrum Imaging for the Measurement of Metal Cutting Temperatures," National Institute of Standards and Technology, Gaithersburg, MD, 2010, http://www.nist.gov/customcf/get_pdf.cfm?pub_id=904301
40. E.P. Whitenton, "Gray Body Calculator," https://pages.nist.gov/rad_calculator/ (accessed November 16, 2022)
41. "Standard for Characterization of Image Sensors and Cameras," EMVA 1288, European Machine Vision Association, 2021
42. B.M. Lane, S. Grantham, H. Yeung, C. Zarobila, and J. Fox, Performance Characterization of Process Monitoring Sensors on the NIST Additive Manufacturing Metrology Testbed, *Proc. Solid Freeform Fabrication Symposium* (Austin, TX), 2017, p 1279–1288, https://www.nist.gov/publications/performance-characterization-process-monitoring-sensors-nist-additive-manufacturing
43. D. Alberts, M. Standfuß, D. Schwarze, and G. Witt, Calibration Approach for Reliable In-Situ Process Monitoring of

Multi-Optic Selective Laser Melting, *Proced. CIRP*, Vol 94, 2020, p 409–413
44. D.C. Deisenroth, S. Mekhontsev, B. Lane, L. Hanssen, I. Zhirnov, V. Khromchenko, S. Grantham, D. Cardenas-Garcia, and A. Donmez, Measurement Uncertainty of Surface Temperature Distributions for Laser Powder Bed Fusion Processes, *J. Res. Natl. Inst. Stand. Technol.*, Vol 126, 2021, p 126013
45. J.C. Heigel, B.M. Lane, and L.E. Levine, In Situ Measurements of Melt-Pool Length and Cooling Rate during 3D Builds of the Metal AM-Bench Artifacts, *Integr. Mater. Manuf. Innov.*, Vol 9 (No. 1), 2020, p 31–53
46. B. Lane, J. Heigel, R. Ricker, I. Zhirnov, V. Khromschenko, J. Weaver, T. Phan, M. Stoudt, S. Mekhontsev, and L. Levine, Measurements of Melt Pool Geometry and Cooling Rates of Individual Laser Traces on IN625 Bare Plates, *Integr. Mater. Manuf. Innov.*, 2020, doi:10.1007/s40192-020-00169-1
47. B. Lane, L. Jacquemetton, M. Piltch, and D. Beckett, "Thermal Calibration of Commercial Melt Pool Monitoring Sensors on a Laser Powder Bed Fusion System," National Institute of Standards and Technology, Gaithersburg, MD, 2020, https://doi.org/10.6028/NIST.AMS.100-35
48. P. Saunders and H. Edgar, On the Characterization and Correction of the Size-of-Source Effect in Radiation Thermometers, *Metrologia*, Vol 46 (No. 1), 2008, p 62–74
49. M.J. Hobbs, C. Zhu, M.P. Grainger, C.H. Tan, and J.R. Willmott, Quantitative Traceable Temperature Measurement Using Novel Thermal Imaging Camera, *Opt. Express*, Vol 26 (No. 19), 2018, p 24904–24916
50. J. Envall, S.N. Mekhontsev, Y. Zong, and L.M. Hanssen, Spatial Scatter Effects in the Calibration of IR Pyrometers and Imagers, *Int. J. Thermophys.*, Vol 30 (No. 1), 2009, p 167–178
51. J.L. McMillan, A. Whittam, M. Rokosz, and R.C. Simpson, Towards Quantitative Small-Scale Thermal Imaging, *Measurement*, Vol 117, 2018, p 429–434
52. "Emissivity Coefficients Common Products," The Engineering Toolbox, https://www.engineeringtoolbox.com/emissivity-coefficients-d_447.html, accessed Jan 6, 2022
53. Y.S. Touloukian and D.P. DeWitt, *Thermal Radiative Properties: Metallic Elements and Alloys*, Plenum Publishing Corporation, New York, NY, 1970
54. M. Boivineau and G. Pottlacher, Thermophysical Properties of Metals at Very High Temperatures Obtained by Dynamic Heating Techniques: Recent Advances, *Int. J. Mater. Prod. Technol.*, Vol 26 (No. 3), 2006, p 217–246
55. L. del Campo, R.B. Pérez-Sáez, L. González-Fernández, X. Esquisabel, I. Fernández, P. González-Martín, and M.J. Tello, Emissivity Measurements on Aeronautical Alloys, *J. Alloy. Compd.*, Vol 489 (No. 2), 2010, p 482–487
56. M. Susa and R.K. Endo, Emissivities of High Temperature Metallic Melts, *High-Temperature Measurements of Materials*, H. Fukuyama and Y. Waseda, Ed., Springer Berlin Heidelberg, 2009, p 111–129, http://link.springer.com/chapter/10.1007/978-3-540-85918-5_6, accessed Dec 13, 2013
57. H. Watanabe, M. Susa, H. Fukuyama, and K. Nagata, Phase (Liquid/Solid) Dependence of the Normal Spectral Emissivity for Iron, Cobalt, and Nickel at Melting Points, *Int. J. Thermophys.*, Vol 24 (No. 2), 2003, p 473–488
58. B. Lane, I. Zhirnov, S. Mekhontsev, S. Grantham, R. Ricker, S. Rauniyar, and K. Chou, Transient Laser Energy Absorption, Co-Axial Melt Pool Monitoring, and Relationship to Melt Pool Morphology, *Addit. Manuf.*, Vol 36, 2020, p 101504
59. R.P. Madding, Emissivity Measurement and Temperature Correction Accuracy Considerations, *Proceedings of the SPIE*, Vol 3700, D.H. LeMieux and J.R. Snell, Jr., Ed., 1999, p 393–401
60. M. Doubenskaia, M. Pavlov, S. Grigoriev, and I. Smurov, Definition of Brightness Temperature and Restoration of True Temperature in Laser Cladding Using Infrared Camera, *Surf. Coat. Technol.*, Vol 220, 2013, p 244–247
61. W. Hofmeister and M. Griffith, Solidification in Direct Metal Deposition by LENS Processing, *JOM*, Vol 53 (No. 9), 2001, p 30–34
62. S. Price, J. Lydon, K. Cooper, and K. Chou, Experimental Temperature Analysis of Powder-Based Electron Beam Additive Manufacturing, *Solid Freeform Fabrication Proceedings* (Austin, TX), 2013, p 162–173
63. S. Price, B. Cheng, J. Lydon, K. Cooper, and K. Chou, On Process Temperature in Powder-Bed Electron Beam Additive Manufacturing: Process Parameter Effects, *J. Manuf. Sci. Eng.*, Vol 136 (No. 6), 2014, p 061019
64. I. Yadroitsev, P. Krakhmalev, and I. Yadroitsava, Selective Laser Melting of Ti6Al4V Alloy for Biomedical Applications: Temperature Monitoring and Microstructural Evolution, *J. Alloy. Compd.*, Vol 583, 2014, p 404–409
65. J. Heigel and B. Lane, Measurement of the Melt Pool Length during Single Scan Tracks in a Commercial Laser Powder Bed Fusion Process, *Proc. 2017 ASME International Conference on Manufacturing Science and Engineering* (Los Angeles, CA), 2017
66. G. Mohr, S. Nowakowski, S.J. Altenburg, C. Maierhofer, and K. Hilgenberg, Experimental Determination of the Emissivity of Powder Layers and Bulk Material in Laser Powder Bed Fusion Using Infrared Thermography and Thermocouples, *Metals*, Vol 10 (No. 11), 2020, p 1546
67. J.C. Heigel, B.M. Lane, and S.P. Moylan, Variation of Emittivity with Powder Bed Fusion Build Parameters, *Proc. Solid Freeform Fabrication Symposium* (Austin, TX), 2016, p 1660–1669
68. J. Haley, C. Leach, B. Jordan, R. Dehoff, and V. Paquit, In-Situ Digital Image Correlation and Thermal Monitoring in Directed Energy Deposition Additive Manufacturing, *Opt. Express*, Vol 29 (No. 7), 2021, p 9927–9941
69. R.J. Williams, A. Piglione, T. Rønneberg, C. Jones, M.-S. Pham, C.M. Davies, and P.A. Hooper, In Situ Thermography for Laser Powder Bed Fusion: Effects of Layer Temperature on Porosity, Microstructure and Mechanical Properties, *Addit. Manuf.*, Vol 30, 2019, p 100880
70. E. Rodriguez, J. Mireles, C.A. Terrazas, D. Espalin, M.A. Perez, and R.B. Wicker, Approximation of Absolute Surface Temperature Measurements of Powder Bed Fusion Additive Manufacturing Technology Using in Situ Infrared Thermography, *Addit. Manuf.*, Vol 5, 2015, p 31–39
71. R.B. Dinwiddie, M.M. Kirka, P.D. Lloyd, R.R. Dehoff, L.E. Lowe, and G. S. Marlow, Calibrating IR Cameras for In-Situ Temperature Measurement during the Electron Beam Melt Processing of Inconel 718 and Ti-Al6-V4, *Thermosense: Thermal Infrared Applications XXXVIII*, International Society for Optics and Photonics, 2016, p 986107, doi:10.1117/12.2229070
72. S. Taylor, J.B. Wright, E.C. Forrest, B. Jared, J. Koepke, and J. Beaman, Investigating Relationship between Surface Topography and Emissivity of Metallic Additively Manufactured Parts, *Int. Commun. Heat Mass Transf.*, Vol 115, 2020, p 104614
73. D.C. Deisenroth, L. Hanssen, and S. Mekhontsev, High Temperature Reflectometer for Spatially Resolved Spectral Directional Emissivity of Laser Powder Bed Fusion Processes, *Reflection, Scattering, and Diffraction from Surfaces VII*, International Society for Optics and Photonics, 2020, p 114850K, doi:10.1117/12.2568179
74. N. Boone, C. Zhu, C. Smith, I. Todd, and J.R. Willmott, Thermal Near Infrared Monitoring System for Electron Beam Melting with Emissivity Tracking, *Addit. Manuf.*, Vol 22, 2018, p 601–605
75. C. Kledwig, H. Perfahl, M. Reisacher, F. Brückner, J. Bliedtner, and C. Leyens, Analysis of Melt Pool Characteristics and Process Parameters Using a Coaxial

Monitoring System during Directed Energy Deposition in Additive Manufacturing, *Materials*, Vol 12 (No. 2), 2019, p 308
76. J. Ye, S.A. Khairallah, A.M. Rubenchik, M.F. Crumb, G. Guss, J. Belak, and M. J. Matthews, Energy Coupling Mechanisms and Scaling Behavior Associated with Laser Powder Bed Fusion Additive Manufacturing, *Adv. Eng. Mater.*, 2019, p 1900185
77. R.B. Dinwiddie, R.R. Dehoff, P.D. Lloyd, L.E. Lowe, and J.B. Ulrich, Thermographic In-Situ Process Monitoring of the Electron-Beam Melting Technology Used in Additive Manufacturing, *Proc. SPIE*, Vol 87050K, 2013, p 87050K–9, http://dx.doi.org/10.1117/12.2018412
78. B. Cheng, S. Price, J. Lydon, K. Cooper, and K. Chou, On Process Temperature in Powder-Bed Electron Beam Additive Manufacturing: Model Development and Validation, *J. Manuf. Sci. Eng.*, Vol 136 (No. 6), 2014, p 061018
79. H. Yeung and B. Lane, A Residual Heat Compensation Based Scan Strategy for Powder Bed Fusion Additive Manufacturing, *Manuf. Lett.*, Vol 25, 2020, p 56–59
80. L. Caprio, A.G. Demir, and B. Previtali, Observing Molten Pool Surface Oscillations during Keyhole Processing in Laser Powder Bed Fusion as a Novel Method to Estimate the Penetration Depth, *Addit. Manuf.*, Vol 36, 2020, p 101470, doi:10.1016/j .addma.2020.101470
81. S.A. Khairallah, T. Sun, and B.J. Simonds, Onset of Periodic Oscillations as a Precursor of a Transition to Pore-Generating Turbulence in Laser Melting, *Addit. Manuf. Lett.*, Vol 1, 2021, p 100002
82. G. Zenzinger, J. Bamberg, A. Ladewig, T. Hess, B. Henkel, and W. Satzger, Process Monitoring of Additive Manufacturing by Using Optical Tomography, *AIP Conference Proceedings* (Boise, ID), American Institute of Physics, 2015, p 164–170, doi:10.1063/1.4914606
83. Z. Liang, I. Zhirnov, F. Zhang, K.K. Jones, D. Deisenroth, M. Williams, U. Kattner, K. Moon, W.-K. Liu, B. Lane, and C. Campbell, Development of Computational Framework for Titanium Alloy Phase Transformation Prediction in Laser Powder-Bed Fusion Additive Manufacturing, *Materialia*, Vol 14, 2020, p 100934, doi:10.1016/j.mtla.2020.100934
84. P.Y. Shcheglov, A.V. Gumenyuk, I.B. Gornushkin, M. Rethmeier, and V.N. Petrovskiy, Vapor-Plasma Plume Investigation during High-Power Fiber Laser Welding, *Laser Phys.*, Vol 23 (No. 1), 2012, p 016001
85. X. Zhang, B. Cheng, and C. Tuffile, Simulation Study of the Spatter Removal Process and Optimization Design of Gas Flow System in Laser Powder Bed Fusion, *Addit. Manuf.*, Vol 32, 2020, p 101049, doi:10.1016/j.addma.2020.101049
86. H. Zheng, H. Li, L. Lang, S. Gong, and Y. Ge, Effects of Scan Speed on Vapor Plume Behavior and Spatter Generation in Laser Powder Bed Fusion Additive Manufacturing, *J. Manuf. Process.*, Vol 36, 2018, p 60–67
87. D.A. Kriczky, J. Irwin, E.W. Reutzel, P. Michaleris, A.R. Nassar, and J. Craig, 3D Spatial Reconstruction of Thermal Characteristics in Directed Energy Deposition through Optical Thermal Imaging, *J. Mater. Process. Technol.*, Vol 221, 2015, p 172–186
88. T. Kolb, R. Elahi, J. Seeger, M. Soris, C. Scheitler, O. Hentschel, J. Tremel, and M. Schmidt, Camera Signal Dependencies within Coaxial Melt Pool Monitoring in Laser Powder Bed Fusion, *Rapid Prototyp. J.*, Vol 26 (No. 1), 2019, p 100–106
89. T. Kolb, L. Müller, J. Tremel, and M. Schmidt, Melt Pool Monitoring for Laser Beam Melting of Metals: Inline-Evaluation and Remelting of Surfaces, *Proced. CIRP*, Vol 74, 2018, p 111–115
90. T. Craeghs, F. Bechmann, S. Berumen, and J.-P. Kruth, Feedback Control of Layerwise Laser Melting Using Optical Sensors, *Phys. Proced.*, Vol 5, 2010, p 505–514
91. E. Vasileska, A.G. Demir, B.M. Colosimo, and B. Previtali, Layer-Wise Control of Selective Laser Melting by Means of Inline Melt Pool Area Measurements, *J. Laser Applic.*, Vol 32 (No. 2), 2020, p 022057
92. H. Yeung, Z. Yang, and L. Yan, A Meltpool Prediction Based Scan Strategy for Powder Bed Fusion Additive Manufacturing, *Addit. Manuf.*, 2020, p 101383
93. Y. Zhang, G.S. Hong, D. Ye, K. Zhu, and J.Y.H. Fuh, Extraction and Evaluation of Melt Pool, Plume and Spatter Information for Powder-Bed Fusion AM Process Monitoring, *Mater. Des.*, Vol 156, 2018, p 458–469
94. H. Zheng, Y. Wang, Y. Xie, S. Yang, R. Hou, Y. Ge, L. Lang, S. Gong, and H. Li, Observation of Vapor Plume Behavior and Process Stability at Single-Track and Multi-Track Levels in Laser Powder Bed Fusion Regime, *Metals*, Vol 11 (No. 6), 2021, p 937
95. D. Yang, H. Li, S. Liu, C. Song, Y. Yang, S. Shen, J. Lu, Z. Liu, and Y. Zhu, In Situ Capture of Spatter Signature of SLM Process Using Maximum Entropy Double Threshold Image Processing Method Based on Genetic Algorithm, *Opt. Laser Technol.*, Vol 131, 2020, p 106371
96. M. Taheri Andani, R. Dehghani, M.R. Karamooz-Ravari, R. Mirzaeifar, and J. Ni, A Study on the Effect of Energy Input on Spatter Particles Creation during Selective Laser Melting Process, *Addit. Manuf.*, Vol 20, 2018, p 33–43
97. C. Lough, R. Landers, D. Bristow, J. Drallmeier, B. Brown, and E. Kinzel, Experiment Based Superposition Thermal Modeling of Laser Powder Bed Fusion, *Proc. Solid Freeform Fabrication Symposium* (Austin, TX), 2021, p 1326–1333
98. G. Mohr, S.J. Altenburg, A. Ulbricht, P. Heinrich, D. Baum, C. Maierhofer, and K. Hilgenberg, In-Situ Defect Detection in Laser Powder Bed Fusion by Using Thermography and Optical Tomography—Comparison to Computed Tomography, *Metals*, Vol 10 (No. 1), 2020, doi:10.3390/met10010103
99. J. Heigel, B. Lane, T. Phan, D. Brown, M. Strantza, and L. Levine, Sample Design and In-Situ Characterization of Cooling Rate and Melt Pool Length during 3D AM Builds of 15-5 and IN625 AM-Bench Artifacts, *Integr. Mater. Manuf. Innov.*, 2019 (Special issue of the AM-Bench 2018 Test Series)
100. L. Meng, B. McWilliams, W. Jarosinski, H.-Y. Park, Y.-G. Jung, J. Lee, and J. Zhang, Machine Learning in Additive Manufacturing: A Review, *JOM*, Vol 72 (No. 6), 2020, p 2363–2377
101. S.S. Razvi, S. Feng, A. Narayanan, Y.-T. T. Lee, and P. Witherell, *A Review of Machine Learning Applications in Additive Manufacturing*, American Society of Mechanical Engineers Digital Collection, 2019, https://doi.org/10.1115/DETC2019-98415
102. A.G. Demir, C. De Giorgi, and B. Previtali, Design and Implementation of a Multisensor Coaxial Monitoring System with Correction Strategies for Selective Laser Melting of a Maraging Steel, *J. Manuf. Sci. Eng.*, Vol 140 (No. 4), 2018, doi:10.1115/1.4038568
103. M. Doubenskaia, M. Pavlov, and Y. Chivel, Optical System for On-Line Monitoring and Temperature Control in Selective Laser Melting Technology, *Key Eng. Mater.*, Vol 437, 2010, p 458–461
104. P. Lott, H. Schleifenbaum, W. Meiners, K. Wissenbach, C. Hinke, and J. Bültmann, Design of an Optical System for the In-Situ Process Monitoring of Selective Laser Melting (SLM), *Phys. Proced.*, Vol 12, 2011, p 683–690
105. U. Thombansen, A. Gatej, and M. Pereira, Process Observation in Fiber Laser-Based Selective Laser Melting, *Opt. Eng.*, Vol 54 (No. 1), 2014, p 011008

106. B. Lane, S. Mekhontsev, S. Grantham, M. Vlasea, J. Whiting, H. Yeung, J. Fox, C. Zarobila, J. Neira, M. McGlauflin, L. Hanssen, S. Moylan, M.A. Donmez, and J. Rice, Design, Developments, and Results from the NIST Additive Manufacturing Metrology Testbed (AMMT), *Proc. 26th Annual International Solid Freeform Fabrication Symposium* (Austin, TX), 2016, p 1145–1160
107. S. Grantham, B. Lane, J. Neira, S. Mekhontsev, M. Vlasea, and L. Hanssen, Optical Design and Initial Results from NIST's AMMT/TEMPS Facility, *Proc. SPIE* (San Francisco, CA), 2016, p 97380S, doi:10.1117/12.2214246

SELECTED REFERENCES

- G.C. Holst, *Testing and Evaluation of Infrared Imaging Systems*, JCD Publishing, Winter Park, FL; SPIE Press, Bellingham, WA, 2008
- P. Saunders, *Radiation Thermometry: Fundamentals and Applications in the Petrochemical Industry*, SPIE Press, 2007
- "Standard for Characterization of Image Sensors and Cameras," EMVA 1288, European Machine Vision Association, 2021
- M. Vollmer and K.-P. Möllmann, *Infrared Thermal Imaging: Fundamentals, Research and Applications*, 2nd ed., Wiley-VCH, Weinheim, Germany, 2018